Surrogate Modeling Based Aeroacoustic Optimization of an eVTOL Propeller in Cruise Flight Conditions

Elias Peter
Master's Student
Technical University
Munich, Munich, Germany

Jan-Arun Faust
Propeller Design Engineer
eRC-System GmbH,
Ottobrunn, Germany

Marco Stuhlpfarrer
VP Technology and
Innovation
eRC-System GmbH,
Ottobrunn, Germany

ABSTRACT

A surrogate-based optimization (SBO) framework was implemented to optimize the aerodynamic efficiency and tonal aeroacoustics of an eVTOL propeller in cruise flight conditions. An exemplary analysis was performed for a parameterized five-bladed propeller geometry, to study the combined influence of the propeller chord, twist, sweep and anhedral distributions on the multi-objective design criteria. The propeller aerodynamics are simulated using a computational fluid dynamics (CFD) model in ANSYS Fluent. The tonal aeroacoustics noise emission is evaluated at multiple receiver locations around the propeller using the Ffowcs-Williams and Hawkings (FWH) acoustics model. To enable a direct comparison with competing designs, all cases are trimmed to the same target thrust condition by iteratively adjusting the rotational speed. Surrogate modeling techniques are utilized to improve the candidate selection process to reduce the number of function evaluations required for the design task and decrease the overall computational cost. The current work discusses the optimization-problem formulation and solution process. Furthermore, insights into three different designs are provided by comparing designs that are generated based on different design targets, namely, maximum aerodynamic efficiency, minimum overall sound pressure level, and a weighted combination of both.

NOTATION

*

Symbols

c Speed of sound, m/s

l_c Local chord length, m

Ma Mach number, –

p Static pressure, Pa

Q Torque, Nm

R Propeller radius, m

Re Reynolds number, –

T Thrust, N

u, v, w Velocity components, m/s

U Flow velocity, m/s

δ_z Blade anhedral offset, mm

δ_y Blade sweep offset, mm

ε_{rel} Relative prediction error, –

η Propulsive efficiency, –

θ Blade pitch angle, deg

ν Kinematic viscosity, m^2/s

ρ Density, kg/m^3

ϕ Inflow angle, deg

Ω Rotational speed, rad/s

*

Acronyms

CFD Computational Fluid Dynamics

DEP Distributed Electric Propulsion

EGO Efficient Global Optimization

EI Expected Improvement

eVTOL electric Vertical Take-off and Landing

FWH Ffowcs-Williams and Hawkings

HPC High-Performance Computing

LHS Latin Hypercube Sampling

MRF Multiple Reference Frame

OASPL Overall Sound Pressure Level

RANS Reynolds Averaged Navier-Stokes

RPM Revolutions Per Minute

SBO Surrogate-Based Optimization

UAM Urban Air Mobility

INTRODUCTION

Recent developments in aviation have been driven by the growing demand for more efficient, sustainable, and versatile aircraft. One of the most notable trends is the emergence of Urban Air Mobility (UAM), which primarily refers to electric-powered aircraft operating within urban environments to address a variety of use cases, ranging from a more efficient transportation solution in congested areas to hospital patient transport (Refs. 1, 2). A key enabler of UAM is the development of electric Vertical Take-Off and Landing (eVTOL) aircraft, which offer the potential for quieter, more efficient, and environmentally friendly transportation (Ref. 1). Despite their promise, eVTOLs and other advanced aerial mobility concepts face critical challenges. Noise pollution is a major concern for the widespread adoption of UAM, as operations will take place in close proximity to residential and commercial areas. Noise emissions are typically dominated by the aerodynamic noise generated by the rotating propeller blades and the corresponding interactional effects involving other aircraft components (Ref. 3). Reducing noise levels is essential to gaining public acceptance and meeting regulatory requirements. Additionally, eVTOLs operate within a limited energy budget due to current battery technology constraints, necessitating highly efficient aerodynamic and propulsion designs.

As of today, the most common types of eVTOL configurations are Multicopters, Vectored Thrust, and Lift + Cruise configurations, which all feature some sort of distributed electric propulsion (DEP) system (Ref. 4). Figure 1 shows the different categories of DEP configurations with an example for each.

Multicopter Lift + Cruise Vectored Thrust

Figure 1. Different types of eVTOL concepts with industry examples: Multicopter: VoloCity (Ref. 5), Lift+Cruise: ERC Charlie (Ref. 2), Vectored Thrust: Joby S4 (Ref. 6)

There are a variety of analytical theories and numerical modeling approaches, which can be used to describe the aerodynamic behavior of a propeller. The selection of the right computational modeling tools, which capture the relevant flow physics accurately and efficiently, is crucial for the design process of any eVTOL propeller. For preliminary analysis and low-complexity configurations, Blade Element Momentum Theory (BEMT) is well suited to describe the propeller aerodynamics in steady hover flight or forward flight conditions (Ref. 7).

To gain insight into detailed flow phenomena and consider the combined effects of blade twist, chord, sweep, and anhedral, Computational Fluid Dynamics (CFD) provides a significantly higher level of fidelity. While computationally more expensive, CFD enables a more extensive analysis of the aerodynamic and aeroacoustic performance of a propeller. Furthermore, CFD simulations have been used to obtain solutions for the flow field for entire eVTOL aircraft configurations (Refs. 8–10), the large mesh sizes of 50 million to 180 million cells resulted in significant computational costs. Such simulations remain essential for understanding complex flow physics and interaction mechanisms, but are rather unsuitable for design optimization tasks as the high simulation times limit the number of feasible iterations. In contrast, CFD applied to isolated propeller configurations significantly reduces the computational effort, due to the smaller domain size and reduced geometry complexity. This makes CFD simulations feasible for the direct integration in the propeller design process, as a higher number of cases can be simulated within a reasonable time (Refs. 11–13).

In recent research, a large number of design studies have been conducted with the goal of optimizing propeller design by utilizing different numerical and experimental approaches. Weitsman and Greenwood (Ref. 14) conducted a study on the aeroacoustic and aerodynamic performance of eVTOL rotors in hover using BEMT combined with an acoustic prediction code. They found that while lowering disk loading improves both acoustics and aerodynamic performance, other design modifications often involve compromises between the two. Bain et al. (Ref. 15) conducted both experimental and computational studies to improve the aerodynamic and aeroacoustic performance of a eVTOL propeller. For computational modeling, low-fidelity lifting-line methods and high-fidelity CFD simulations were used to assess the aerodynamic and aeroacoustic characteristics. Rapid composite manufacturing of propeller blades allowed them to integrate experimental testing into their design process. Marinus et al. (Ref. 12) conducted a study on the aeroacoustic and aerodynamic optimization of transonic aircraft propeller blades. The research employed a multi-objective differential evolution algorithm in combination with an artificial neural network as the optimization method. RANS simulations were used for the evaluation of propeller designs. The optimized designs numerically demonstrated overall noise reduction and improved aerodynamic efficiency. Klimczyk et al. (Ref. 11) optimized the aerodynamic and acoustic behavior of an eVTOL propeller blade geometry in hover flight. RANS-based CFD simulations were used to assess the aerodynamics and tonal aeroacoustics of the individual designs. A Surrogate-Based Optimization (SBO) approach was employed, enabling reasonable convergence in the optimization process while limiting the number of required design evaluations. SBO has shown to be particularly promising by enabling a highly efficient exploration of the propeller blade parameter space. This leads to a more effective optimization process, requiring fewer iterations to achieve optimal results. As a result, it allows the use of more computationally expensive evaluation methods, which in return capture the underlying physical effects with higher accuracy.

The work presented in this paper discusses the development and application of a customized SBO framework for the design of an eVTOL propeller in cruise flight conditions. The method leverages high-fidelity computational methods to identify designs that maximize performance and minimize noise emissions.

OPTIMIZATION OBJECTIVE AND TESTCASE DESCRIPTION

The implemented method is intended for detailed design work, in which the blade geometry is defined in accordance with design constraints, including the cruise velocity, blade count, diameter, and thrust requirement. By utilizing a surrogate model to approximate the relation between the propeller geometry and its aerodynamic and aeroacoustic behavior, an efficient design candidate selection is enabled. The optimization framework focuses on achieving a balance between the following global objectives:

- Maximizing propeller propulsive efficiency: η
- Minimizing emitted maximum overall sound pressure level: $OASPL_{max}$
- Minimizing a combined objective: $crit_{comb}$

The propulsive efficiency of a propeller in axial forward flight is defined as:

$$\eta = \frac{TU_\infty}{\Omega Q} \tag{1}$$

where the propeller rotational speed is denoted by Ω in rad/s, the generated thrust by T and the torque by Q. The design is optimized for either one of these objectives. An additional combined objective between efficiency and noise is also introduced. For this study, it was defined as:

$$crit_{comb} = \frac{OASPL_{max} - OASPL_{target}}{5dBA} - \frac{\eta - \eta_{target}}{0.02} \tag{2}$$

It evaluates how far a design deviates from target values for efficiency ($\eta_{target} = 0.8$) and sound pressure level ($OASPL_{target}$ = 36dBA). This formulation implies that a 5 dBA noise reduction is seen as equivalent to an efficiency improvement of 2%. The sum of these normalized deviations provides a single performance metric that is to be minimized.

As the focus in this study is primarily on the development of the optimization framework and evaluation of the implemented method, a relatively simple flow case was chosen. A propeller operating under axial inflow conditions in forward flight is analyzed. A flight velocity U_∞ of 50 m/s is assumed to correspond to a typical eVTOL cruise speed. The propeller radius is defined as 0.9 m and a number of 5 blades is prescribed. To enable a direct comparison between competing blade designs, the different propellers are to be trimmed to a specific target thrust by keeping the operating rotational speed as a free parameter and adjusting it to match the design constraints. For this study, the target thrust is set to 1250 N. An overview of the testcase conditions is listed in the Table 1.

Table 1. Testcase conditions

Quantity	[-]
Cruise velocity U_∞	$50\ \mathrm{m/s}$
Inflow angle ϕ	$0\ ^\circ$
Propeller radius R	$0.9\ \mathrm{m}$
No. of blades	5
Target thrust	$1250\ N$

The blade geometry is defined by a total of 12 parameters across three radial positions: 0.1R, 0.7R, and 1.0R. These control points are located on the 1/4 chord line of the propeller blade and are connected by a fourth-order spline interpolation. At each control point, the pitch angle θ, chord length l_c, and positional displacements, sweep in the y-direction δ_y, anhedral in the z-direction δ_z, are defined. This geometric blade definition is visualized in Fig. 2.

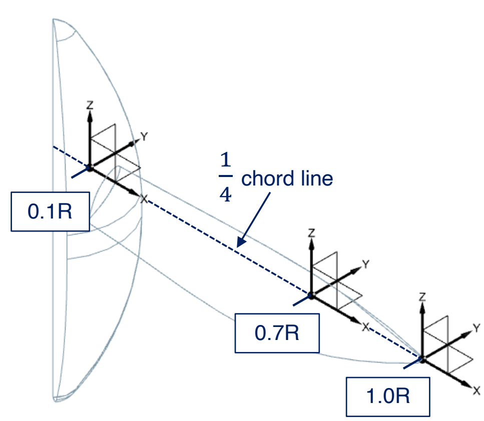

Figure 2. Parameterized propeller geometry

Six of the 12 parameters are set to a fixed value, while the other six remain free and represent open design parameters. At 0.1R all four parameters are fixed, while at 0.7R pitch and chord are free. At 1.0R all four parameters are free. The chosen parametrization enables the study of different pitch and chord distributions, with the combined influence of propeller tip anhedral and sweep. One goal of this selection is to consider as many geometry effects as possible on aerodynamic and aeroacoustic performance while minimizing the number of free parameters. The following Table 2 summarizes the fixed and free parameters considered in the analysis.

Table 2. Propeller geometric parameters

Pos.	Status	Parameter	Design Range
0.1R	fixed	pitch: $\theta_{0.1R}$	55°
	fixed	chord: $l_{c,0.1R}$	100mm
	fixed	anhedral: $\delta_{z,0.1R}$	0mm
	fixed	sweep: $\delta_{y,0.1R}$	10mm
0.7R	free	pitch: $\theta_{0.7R}$	[15°; 45°]
	free	chord: $l_{c,0.7R}$	[100mm; 200mm]
	fixed	anhedral: $\delta_{z,0.7R}$	0mm
	fixed	sweep: $\delta_{y,0.7R}$	10mm
1.0R	free	pitch: $\theta_{1.0R}$	[5°; 30°]
	free	chord: $l_{c,1.0R}$	[15mm; 75mm]
	free	anhedral: $\delta_{z,1.0R}$	[-80mm; 0mm]
	free	sweep: $\delta_{y,1.0R}$	[-150mm; 0mm]

For studies leading up to the selection of the parameter ranges, a baseline geometry was utilized. The geometric definition of the baseline propeller blade with respect to the parameter ranges is depicted in Fig. 3.

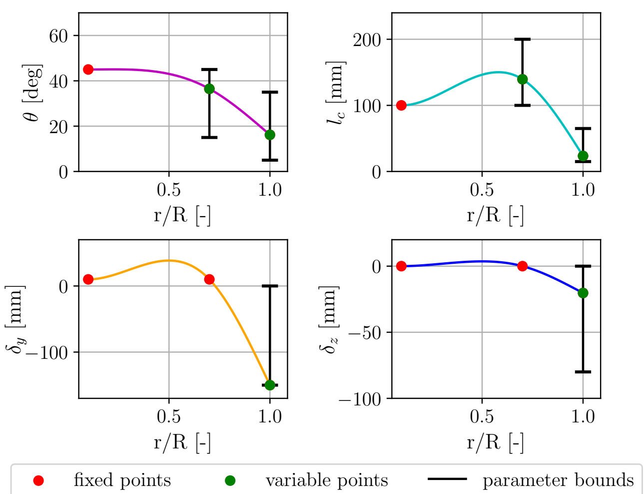

Figure 3. Geometric parameters of baseline propeller geometry

The baseline geometry represents a simplified blade shape, where no anhedral or sweep was applied. The RPM was adjusted to roughly match the design thrust. Initially, the root pitch $\theta_{0.1R}$ was set to 45° for the baseline geometry, which was prone to blade stall on the lower blade surface. For the optimization process, the root pitch was therefore increased to 55°.

To further simplify the optimization process, the airfoil geometry is prescribed at each radial station for all blade designs. It is important to select appropriate airfoil geometries that ensure robust performance over a wide range of Reynolds and Mach numbers, and to be suitable for different blade designs.

The local Reynolds Number at each blade section is defined as:

$$Re = \frac{U l_c}{\nu} \tag{3}$$

where U is the local flow velocity relative to the propeller blade, l_c the local chord length and ν the kinematic viscosity. The flow velocity U is roughly approximated as

$$U = \sqrt{U_\infty^2 + (\Omega r)^2} \tag{4}$$

where the influence of the induced velocity is neglected for simplicity. The Mach Number is defined as:

$$Ma = \frac{U}{c} \tag{5}$$

where c is the speed of sound of the flow medium. The sea-level conditions according to the International Standard Atmosphere (ISA) were used to determine the fluid properties of the air, $c = 340.3 \frac{m}{s}$ and $\nu = 1.461 \cdot \frac{m^2}{s}$. The Table 3 summarizes the airfoils chosen at each design point and the corresponding Re and Ma number ranges. For the calculation of the characteristic Reynolds and Mach numbers, a possible propeller rotational speed range of 1000 to 2100 RPM was postulated.

Table 3. Blade airfoil selection, airfoil geometries taken from (Ref. 16)

Pos.	Airfoil	Ma range	Re range
0.1R	MH126	$0.15 - 0.16$	$3.5 \cdot 10^5 - 3.7 \cdot 10^5$
0.7R	MH114	$0.24 - 0.43$	$1.1 \cdot 10^5 - 2.0 \cdot 10^6$
1.0R	MH116	$0.31 - 0.60$	$1.1 \cdot 10^5 - 1.0 \cdot 10^6$

Prescribing the airfoil geometries reduces the total number of design variables and minimizes the risk of any discrete discontinuities in the objective functions introduced by using different airfoils.

NUMERICAL MODELING

Computational Fluid Dynamics (CFD)

In this study, CFD is used to simulate the aerodynamic characteristics of different propeller designs. Due to the steady operating conditions associated with axial flow, Reynolds-Averaged Navier-Stokes (RANS) based simulations are used in this work. For turbulence modeling, the two-equation Shear-Stress Transport (SST) $k-\omega$ model is applied (Ref. 17). To account for the propeller's rotational speed, a Multiple Reference Frame (MRF) is employed, where the propeller is rotated at a constant speed, and the flow equations in this region are solved in a rotating reference frame. Compressibility effects are considered by using an ideal gas approximation for air as the flow medium.

Boundary Conditions The boundary conditions for this propeller application were selected to provide an accurate and robust simulation setup. The fluid domain is illustrated in Fig. 4.

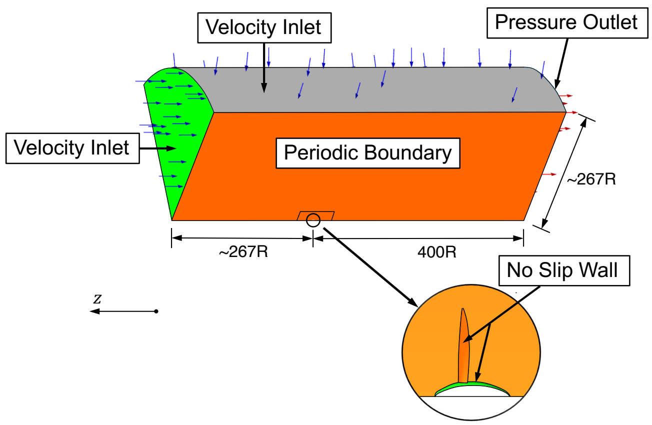

Figure 4. Propeller CFD fluid domain and boundary conditions

A large enough fluid domain around the propeller ensures a full development of the surrounding flow, including the propeller wake, with minimal boundary interference. Upstream of the propeller and on the outer sides of the fluid domain, a velocity inlet boundary condition is applied. This condition is based on the assumption of a fully axial and undisturbed flow at the outermost region of the fluid domain. Furthermore, using a velocity inlet on the outer boundary was found to result in a more stable convergence behavior compared to a pressure outlet boundary. Downstream of the propeller, at the outlet surface, a pressure outlet boundary condition is applied. The blade and hub surfaces of the propeller are modeled as no-slip walls. On the faces of each periodic section, a periodic boundary condition is applied. By utilizing a MRF for a rotational symmetric flow, only a section of the entire domain needs to be modeled and resolved. A single blade is simulated, with the flow solution then being periodically replicated around the rotation axis. Consequently, the CFD simulation represents idealized periodic flow conditions and cannot account for any flow variations between different propeller blades resulting from unsteady flow effects throughout a blade revolution.

Mesh Setup / Grid Resolution The fluid volume was discretized using a poly-hexcore mesh, combining polyhedral cells near boundaries and hexahedral cells in the free field fluid domain. Cells with hanging nodes are used to transition into larger hexahedral cell sizes in the outer domain. To determine an appropriate mesh setup for the optimization, a grid independence study was conducted using three different grid resolutions. The medium resolution, offering the best trade-off between accuracy and computational cost, is used throughout the remainder of the study. A total of 40 prism layers are added to the surfaces of the propeller hub and blade surfaces. The cells within these layers feature a growth rate of 1.2. A first cell height of $1.8 \cdot 10^{-6}\mathrm{m}$ is prescribed. These settings ensure that the boundary layers at the walls are accurately resolved. These key mesh characteristics are summarized in Table 4.

Table 4. Key features of the mesh

Feature	Medium Mesh
Cell type	Poly-Hexcore
Prism layer first cell height	$1.8 \cdot 10^{-6}$ m
Number of cells in prism layer	40
Total cell count[a,b]	8.1M
Prism layer growth rate	1.2
$y^{+}_{\max}$ [a]	1.38
Meshing time[a,b]	17 min

[a]Data obtained using the baseline propeller geometry.
[b]Meshing was performed locally using 4 cores in parallel.

The grid resolution resulted in a low y^+ value across the blade surface, ensuring that the viscous sublayer is resolved. Fig. 5 shows a y^+ contour plot of the mesh at the blade top surface for the respective grid resolutions. In Fig. 6 the mesh of the fluid domain surrounding the propeller blade and its wake is depicted.

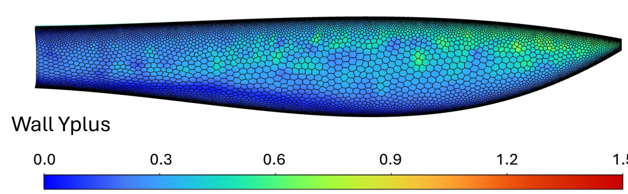

Figure 5. Blade surface mesh with y^+ contour plot

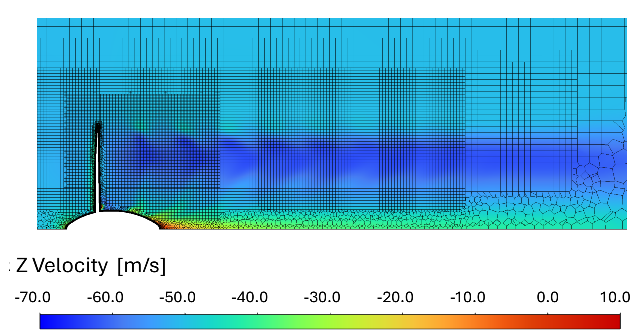

Figure 6. Propeller wake mesh with z-velocity visualized in the xz-plane

Multiple bodies of influence were incorporated in the mesh to ensure a higher wake resolution near the propeller blade and hub. The resolution is incrementally coarsened further away from the propeller.

Propeller Trim Procedure

To enable an effective comparison between any propeller designs, they must be analyzed under operating conditions, which achieve the same constant target thrust. Determining the required propeller RPM to reach this thrust is a process known as trimming. Other studies, such as Klimczyk et al. (Ref. 11), incorporated this step into the surrogate model directly and did not trim the propeller to a target thrust beforehand. To minimize the number of open parameters in the optimization process, the decision was made to perform trimming during the design evaluation. A pre-existing trim method, developed at eRC-System, was utilized and adapted to the current simulation model. While the simulation in ANSYS is running, incremental adjustments to the RPM are made. After an adjustment, the RPM value remains fixed until a stable solution is reached, after which the next trimming step is performed. The adjustment process continues until the target thrust is reached and the RPM is not modified anymore. To extract the results from the trimmed simulation and smooth out the oscillations, a 50-iteration moving average is applied.

Aeroacoustic Model

The human perception of annoyance of a sound heavily depends on its frequency. The most common metric for measuring perceived loudness of a sound is the so-called A-weighting (Ref. 18). To account for this , the A-weighting is used for the quantification of aeroacoustic noises in this work. For the evaluation of tonal aeroacoustic noise in the far-field, most commonly, the Ffowcs Williams-Hawkings (FWH) model is used to predict tonal noise (Refs. 3,11,13,15,19). The FWH model allows for a computation of the far-field acoustic emission of a moving surface and the propagation to a specified observer position. A detailed description of the derivation can be found in (Ref. 18). Under the assumption of linear acoustics, viscous effects are assumed to be negligible and nonlinear terms are dropped from the FWH formulation. If the evaluated surface is selected to be an impenetrable wall, e.g. the propeller blade surface, the formulation further simplifies, leading to the following equation:

$$\begin{aligned} \rho'(\mathbf{x},t)c_\infty^2 H_s = &-\frac{\partial}{\partial x_i}\int_{S_o}\left[\frac{p_{ij}n_j}{4\pi r|1-M_r|}\right]_{\tau=\tau^*} dS \\ &+\frac{\partial}{\partial t}\int_{S_o}\left[\frac{\rho_\infty V_j n_j}{4\pi r|1-M_r|}\right]_{\tau=\tau^*} dS \end{aligned} \tag{6}$$

The different terms of the FWH describe different mechanisms of source generation. The first term of Equation 6 is referred to as the loading noise term:

$$(p'(\mathbf{x},t))_{loading} = -\frac{\partial}{\partial x_i}\int_{S_o}\left[\frac{p_{ij}n_j}{4\pi r|1-M_r|}\right]_{\tau=\tau^*} dS \tag{7}$$

It results from the periodic aerodynamic forces exerted by the blade on the air, as perceived relatively by the observer. The second term of Equation 6 is referred to as the thickness noise term:

$$(p'(\mathbf{x},t))_{thickness} = \frac{\partial}{\partial t}\int_{S_o}\left[\frac{\rho_\infty V_j n_j}{4\pi r|1-M_r|}\right]_{\tau=\tau^*} dS \tag{8}$$

The thickness noise arises from the displacement of the fluid by the moving surface, such as the spinning propeller blade. To a stationary observer, the apparent volume of the blade changes over time with its rotation. This mechanism generates a sound wave, emitted into the far-field (Ref. 18).

For the concrete evaluation of the aeroacoustics of the propeller in this work, ANSYS Fluent's implementation of the FWH equation was used to predict tonal noise. The steady-state solution is used to predict far-field noise emissions as the FWH method can capture tonal noise from a steady-state simulation in case a MRF is used. The OASPL levels are evaluated at specific receiver positions in the far-field. The receivers were evenly spaced around the propeller between 0 and 180 degrees around the propeller plane in steps of 10 degrees. A constant distance of $12m$ was selected. The receiver arrangement is visualized in Fig 7.

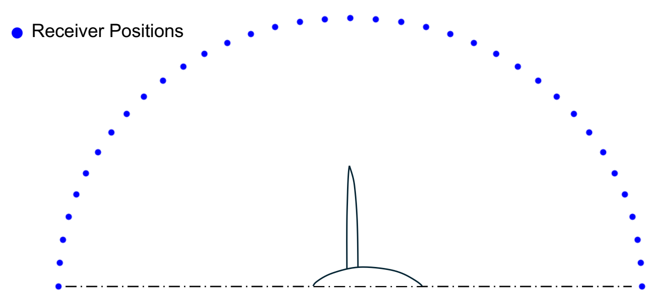

Figure 7. Receiver positions around propeller plane (not to scale)

For the evaluation of the OASPL of a design in the optimization process, the maximum OASPL value out of all the receivers is used, as opposed to a specific source location, as this could change depending on the blade shape. This value is described as $OASPL_{max}$.

To consider broadband noise stemming from unsteady turbulent effects, there are a variety of additional tools, most notably the Brook, Pope and Marcolini Model (BPM) (Ref. 20), a semiempirical prediction method for airfoil self-noise. The broadband prediction model in ANSYS Fluent currently does not have the capability to predict noise emissions in the far-field. Hence, no broadband model was utilized, and only the tonal noise contributions were computed in this study.

SURROGATE BASED OPTIMIZATION FRAMEWORK

Surrogate Model Setup

Surrogate modeling is an approach used in engineering and science to approximate complex simulations or experiments. Instead of running computationally expensive simulations for every evaluation, a surrogate model is trained using input-output data from a limited number of strategically chosen points. The surrogate model can quickly approximate new design points while maintaining sufficient accuracy (Ref. 21).

General Optimization Workflow The general unspecific optimization problem is formulated as follows:

$$\begin{aligned} \text{Minimize:} \quad & y = f(\mathbf{x}) \quad \text{with respect to } \mathbf{x}, \\ \text{subject to:} \quad & x_i \in [0,1]. \end{aligned} \tag{9}$$

where the input data $\mathbf{x}$ is inserted into the expensive function evaluation f to obtain the output data $\mathbf{y}$. In general, surrogate-based optimization consists of the following steps:

1. Select initial sample designs
2. Evaluate selected designs
3. Train surrogate model
4. Select the next candidates using the surrogate
5. Go back to step 2

These steps are repeated until either a desired number of designs has been evaluated or a pre-defined convergence criterion has been reached.

Initial Sampling Strategy For the selection of the initial sample, it is desired to explore the design space as efficiently as possible. Therefore, choosing an appropriate sampling method is essential. In this study, the initial designs were selected with the Latin Hypercube Sampling (LHS) method. The LHS method is widely recommended for surrogate modeling due to its ability to ensure a well-distributed and space-filling sample across multiple dimensions (Ref. 22). Unlike simple random sampling, LHS avoids clustering of points in the design space, leading to a more evenly spread-out sample set. A detailed description of the LHS method can be found in (Ref. 21).

Gaussian Process Regression (Kriging) A large number of surrogate models are available for optimization tasks, including, among others, polynomial functions, radial basis functions, and artificial neural networks. The choice of method depends on the problem formulation and the number of available data points. Gaussian process regression, often also referred to as Kriging, is the surrogate model method used in this work. The basic model can be expressed as follows, adopted from (Ref. 23) and (Ref. 24):

$$\hat{y} = \rho^T(\mathbf{x}) \cdot \beta + Z(\mathbf{x}) \tag{10}$$

The, by the Kriging model predicted function value, is denoted as $\hat{y}$, obtained from the n-dimensional input vector $\mathbf{x} \in \mathbb{R}^n$. A number of m, typical polynomial basis functions $\rho(\mathbf{x}) = [\rho_1(x), ..., \rho_m(x)]^T$ are weighted by the regression coefficient vector $\beta = [\beta_1, ..., \beta_m]^T$. For the specific model used in this work, $\rho(\mathbf{x})$ only consists of a single constant term as the only basis function. The stochastic process $Z(\mathbf{x})$ features a zero mean and covariance and can be expressed as:

$$cov\left[Z(\mathbf{x}_i), Z(\mathbf{x}_j)\right] = \sigma^2 R(\mathbf{x}_i, \mathbf{x}_j) \tag{11}$$

where σ^2 describes the variance of the stochastic process and $R(\mathbf{x}_i, \mathbf{x}_j)$ is the correlation function of the inputs $\mathbf{x}_i$ and $\mathbf{x}_j$. For a Gaussian correlation $R(\mathbf{x}_i, \mathbf{x}_j)$ can be defined as:

$$R(\mathbf{x}_i, \mathbf{x}_j) = \prod_{l=1}^{n} \exp\left(-\theta_l \left(x_{i,l} - x_{j,l}\right)^2\right), \quad \theta_l \in \mathbb{R}^+ \tag{12}$$

The hyperparameters θ_l are used to tune $R(\mathbf{x}_i, \mathbf{x}_j)$ and control the rate of correlation in each input dimension. To train the actual Kriging model, k data points with their respective inputs $\mathbf{x} = [\mathbf{x_1}, ..., \mathbf{x_k}]^T$ and outputs $\mathbf{y} = [\mathbf{y_1}, ..., \mathbf{y_k}]^T$ are required. The hyperparameters θ_l are estimated by applying a maximum likelihood estimation, solving the following equation:

$$\hat{\theta}_l = \arg\max_{\theta_l}\{-\frac{k}{2}\ln(\hat{\sigma}^2) - \frac{1}{2}\ln(|\mathbf{R}|)\} \tag{13}$$

where the regression coefficient is estimated β as:

$$\hat{\beta} = (\rho_D^T \mathbf{R}^{-1} \rho_D)^{-1} \rho_D^T \mathbf{R}^{-1} \mathbf{y} \tag{14}$$

and the variance σ^2 as:

$$\hat{\sigma}^2 = \frac{1}{k}\left(\mathbf{y} - \rho_D \hat{\beta}\right)^T \mathbf{R}^{-1} \left(\mathbf{y} - \rho_D \hat{\beta}\right) \tag{15}$$

with $\rho_D = [\rho(\mathbf{x}_1), \cdots, \rho(\mathbf{x}_k)]^T$ being an $k \times m$ matrix consisting of the basis functions evaluated at the $\mathbf{x}$ inputs of the k data points. The matrix $\mathbf{R}$ is made up of the correlation functions $R(\mathbf{x}_i, \mathbf{x}_j)$ and is referred to as the correlation matrix. Once the hyperparameters θ_l are found and the model is trained, it can predict an output $\hat{y}$ for an arbitrary input point $\mathbf{x}^*$, using the following equation:

$$\hat{y} = \hat{f}(\mathbf{x}^*) = \rho^T(\mathbf{x}^*)\hat{\beta} + \mathbf{r}_0^T \mathbf{R}^{-1}\left(\mathbf{y} - \rho_D \hat{\beta}\right) \tag{16}$$

The correlations between the unobserved point x^* and the already evaluated points $\mathbf{x} = [\mathbf{x_1}, ..., \mathbf{x_k}]^T$ are given by $\mathbf{r}_0 = [R(\mathbf{x}_1, \mathbf{x}^*), \ldots, R(\mathbf{x}_k, \mathbf{x}^*)]^T$. A big advantage of the Kriging model approach is its capability of predicting the uncertainty within the surrogate at any unobserved input point $\mathbf{x}^*$. The following equation describes the variance of the prediction:

$$s^2(\mathbf{x}^*) = \hat{\sigma}^2 \Big[1 - \mathbf{r}_0^\top \mathbf{R}^{-1} \mathbf{r}_0 + \left(\rho(\mathbf{x}^*) - \rho_D^\top \mathbf{R}^{-1} \mathbf{r}_0\right)^\top \left(\rho_D^\top \mathbf{R}^{-1} \rho_D\right)^{-1} \left(\rho(\mathbf{x}^*) - \rho_D^\top \mathbf{R}^{-1} \mathbf{r}_0\right) \Big] \quad (17)$$

The uncertainty increases as the evaluated points move further away from the training data, while it vanishes at the location of the training data itself.

Noise Handling Unfortunately, in many real-life applications, errors are often introduced in the evaluation of the objective function. These errors may arise from measurement inaccuracies in experiments or numerical inaccuracies in simulations. Additionally, the presence of noise in the results may also arise from inherent physical effects, as the underlying physical phenomena may not necessarily lead to smooth function curves. The function evaluation with noisy data can be formulated as:

$$y = f(\mathbf{x}) + \varepsilon_l, \quad l = 1, ..., k. \quad (18)$$

where the additional error introduced by the noise for each data point is denoted as ε_l. The standard Kriging model can be extended to account for a noise term.

$$\hat{y} = \rho^T(\mathbf{x}) \cdot \beta + Z(\mathbf{x}) + \varepsilon_l \quad (19)$$

In the case of homoscedastic noise, the noise variance is assumed to be constant across all samples and can be estimated using maximum likelihood. To account for noise in the surrogate prediction, the noise variance must be added to the diagonal of the correlation matrix R in Equation 16. A detailed derivation of this modification can be found in (Ref. 25). The impact of noise handling is illustrated using a simple example dataset in Fig. 8, generated using the SMT Toolbox (Ref. 26).

This example illustrates how noisy data can become problematic for the standard Kriging model if many function evaluation points are in close proximity. Since the standard Kriging model fits exactly through each data point, it may result in abrupt variations in the surrogate model due to overfitting. As a consequence, inaccuracies may arise, such as overpredicting the function value, which could impact the optimization convergence behavior. However, in areas where function evaluations are more sparse and widely distributed, the surrogate model is less influenced by the absence of noise handling (see Fig. 8).

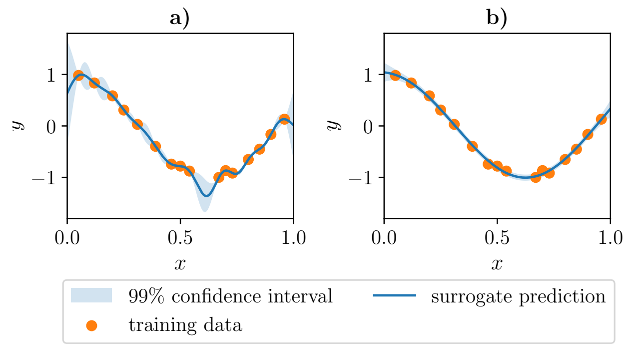

Figure 8. Comparison of Kriging models trained on the same noisy dataset: without noise handling: a), with noise handling: b)

Exploration versus Exploitation After the sampling points have been evaluated, individual candidates are selected iteratively using the surrogate model. In the previous section, the capability of the Kriging model to predict the uncertainty of the surrogate model was shown. This information can be incorporated into the selection of the next candidates in the optimization process, allowing for a strategic choice between increasing the model's certainty or optimizing the objective function. The balance between these two approaches is known as exploration versus exploitation. Exploration focuses on exploring uncertain regions of the design space, increasing the likelihood of finding the global optimum. In contrast, exploitation refines areas with already promising results, but at the risk of getting stuck in local minima. To effectively balance exploration and exploitation, the Expected Improvement (EI) metric, which forms the foundation of the Efficient Global Optimization (EGO) method (Ref. 27), is commonly used. First of all, we can define the improvement at a point $\mathbf{x}$ as:

$$I(\mathbf{x}) = \max(f_{min} - Y, 0) \quad (20)$$

where the current best function value is f_{min}, and Y which is a normally distributed random variable. It represents the predicted function value at $\mathbf{x}$, modeled as a normally distributed random variable with mean $\hat{y}$ and variance s^2. Then EI simply can be expressed as:

$$E[I(\mathbf{x})] = E[\max(f_{min} - Y, 0)] \quad (21)$$

EI provides a measure of how much improvement a new candidate point is expected to yield over the current best observed value. EI can be computed using the following equation:

$$E[I(\mathbf{x})] = (f_{\min} - \hat{y})\Phi\left(\frac{f_{\min} - \hat{y}}{s}\right) + s\phi\left(\frac{f_{\min} - \hat{y}}{s}\right) \quad (22)$$

In this context $\phi(\cdot)$ and $\Phi(\cdot)$ describe the standard probability density function and the cumulative distribution functions, respectively. More details regarding EI and its derivation can be found in (Ref. 27).

Framework Development

A flow diagram of the implementation of the surrogate-based optimization for the multi-objective optimization of the propeller design is depicted in Fig. 9. The general workflow is comparable to the one used by Klimczyk et al. (Ref. 11).

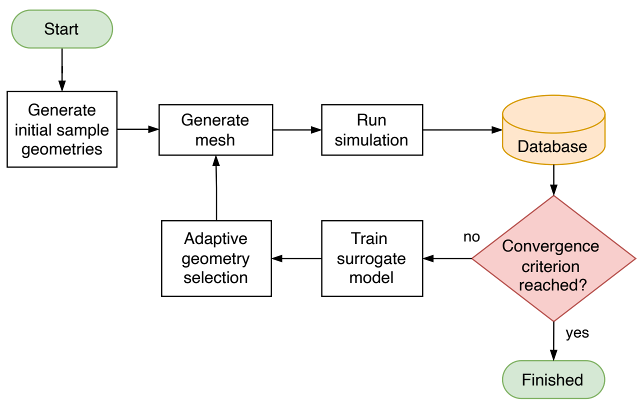

Figure 9. Optimization workflow

The process begins with the generation of the initial set of design samples, defining the geometric parameters of the propeller. Based on the chosen parameters, the geometries are created and the corresponding mesh is generated. Once completed, the meshes are sent to a dedicated Linux High-Performance Computing (HPC) cluster, where the CFD simulations are performed. After a simulation run has finished, the essential results are sent back to the local machine and saved in a database. Once the evaluation of the samples is completed, the adaptive geometry selection is started. A specific surrogate model is trained for each optimization objective, meaning $OASPL_{max}$, η, and $crit_{comb}$. At each iteration, new candidates are selected by using the respective surrogate. The selected candidates are then reintroduced into the workflow, undergoing geometry generation, meshing, simulation, and postprocessing in a continuous iterative cycle. This process is repeated until either the desired number of total candidates has been reached or a defined convergence criterion has been met.

A Python framework was developed to facilitate the interaction between the required software tools and to allow for an automated optimization procedure. The user is required to generate a template CAD, mesh, and setup files, which are updated automatically in Python for the consequent design iterations. The mesh is first transferred from the local machine to the HPC system, where the simulation is executed. Upon completion, the simulation data is post-processed, and only the essential results are sent back. The relevant input-output data for the optimization is then stored in a database on the local machine. For all surrogate modeling tasks, the SMT Toolbox (Ref. 26) is utilized. The surrogate model is built on the local machine, where the surrogate evaluation and adaptive candidate selection are performed.

AEROACOUSTIC OPTIMIZATION

Initial Sample

The goal of selecting the initial sample designs is to provide enough information for the surrogate model to develop an initial understanding of the design space. With this foundation, the surrogate can efficiently search for optima during the adaptive process. A total of 60 samples were generated using the LHS method, corresponding to 10 times as many samples as open parameters, as suggested by Loeppky et al. (Ref. 28). Some selected geometries from the initial sample set are shown in 10.

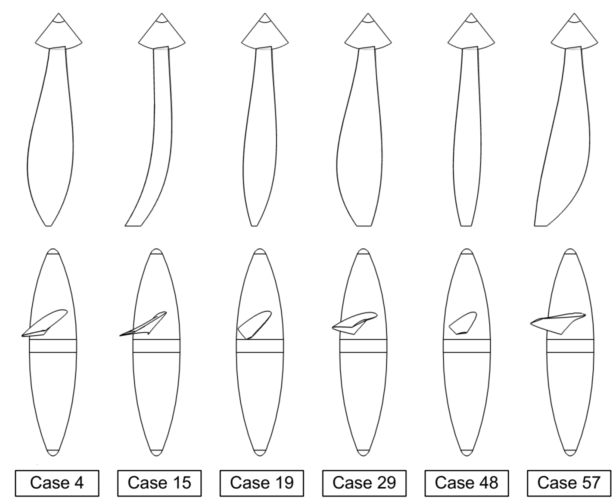

Figure 10. Variety of selected sample geometries shown in top and side view

The input values were normalized from 0 to 1, representing the corresponding lower and upper bounds. It is to be noted that both during the initial sampling process and the adaptive optimization step, certain propeller designs resulted in poor-quality meshes with low-quality cells. To address this, minor adjustments were made to the mesh setup for these cases in particular, without significantly affecting the flow domain grid resolution. This highlights the challenges associated with automating the generation of robust meshes for CFD.

Adaptive Optimization

After the initial samples were evaluated, the obtained data was used to train a surrogate for each of the three optimization variables, η, $OASPL$ and the $crit_{comb}$. The respective surrogate is then used to select a set of new designs for each iteration within the adaptive infill procedure. In this study, a new design was selected for each of the following concrete conditions:

- Maximizing η
- Maximizing EI of η
- Minimizing $OASPL_{max}$
- Maximizing EI of $OASPL_{max}$
- Minimizing $crit_{comb}$
- Maximizing EI of $crit_{comb}$

For finding these design points within the surrogate, the differential evolution (DE) algorithm from the SciPy Python package (Ref. 29) was used. A combination of direct objective optimization and EI was previously used by Klimczyk et al. (Ref. 11). This hybrid approach offers an adjusted exploration–exploitation trade-off, with a stronger focus on exploitation by also directly trying to find the optimum.
Additionally, a constraint of a minimum euclidean distance of 0.01 between any two design points was incorporated into the selection of new design points:

$$\begin{aligned} d_{\min} &= \min \left\| \mathbf{x}_i - \mathbf{x}_j \right\|, \quad \forall i,j \in \{1,\ldots,k\}, i \neq j \\ \left\| \mathbf{x}_i - \mathbf{x}_j \right\| &= \sqrt{\sum_{l=1}^{6} \left(x_{i,l} - x_{j,l}\right)^2} \\ d_{\min} &> 0.01 \end{aligned} \tag{23}$$

This was included to avoid dense clustering of designs at highly localized points within the design space. A total of 20 infill iterations with 6 newly selected designs per iteration were performed. Together with the sample designs, this resulted in a number of 180 evaluated propeller designs. Initially, the noise handling feature of the surrogate model was turned off as it was expected that the design points would be sufficiently spaced apart for noisy data to not have a significant influence.
An increasing prediction error between the actual objective function values and the surrogate model predictions during successive infill iterations was observed, which was attributed to noisy data worsening the accuracy of the surrogate. Therefore, homoscedastic noise handling was incorporated into the surrogate model for all subsequent iterations, starting after the 11th infill iteration. The respective relative errors were determined the following way:

$$\begin{aligned} \varepsilon_{rel,\eta} &= \frac{|\hat{y}_\eta - y_\eta|}{0.02} \\ \varepsilon_{rel,OASPL_{max}} &= \frac{|\hat{y}_{OASPL_{max}} - y_{OASPL_{max}}|}{5dBA} \\ \varepsilon_{rel,crit_{comb}} &= |\hat{y}_{comb} - y_{comb}| \end{aligned} \tag{24}$$

The normalized error is based on the consideration of the combined criterion $crit_{comb}$ to obtain a comparable scaling between $OASPL_{max}$ and η. The relative error of the combined metric $crit_{comb}$ does not include a fractional term because by its definition (Eq. 2) it is already a relative value. The evolution of the relative prediction error of each optimization variable over the infill iterations is shown in Fig. 11.

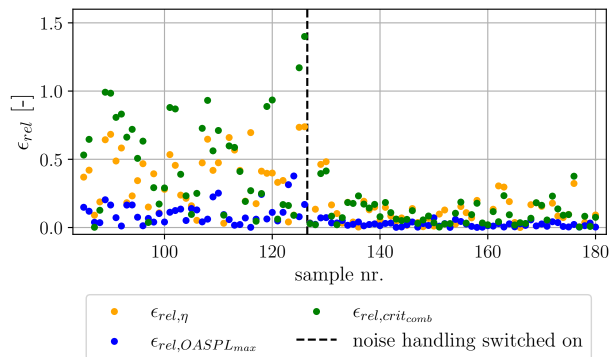

Figure 11. Relative prediction error of surrogate model during adaptive infill process, before and after noise handling

There are multiple sources which could contribute to noisy aeroacoustic and aerodynamic data. Numerical noise due to oscillatory CFD solution behavior can influence the results, even after applying a moving-average. Insufficient trim accuracy, particularly evident in designs that are subject to large scale flow separation, also contributes to additional variance in the output data. A significant increase in surrogate prediction accuracy was observed once noise was considered, leading to an improvement in design candidate selection and overall convergence of the optimization. The prediction error of $crit_{comb}$ and η is generally significantly higher compared to $OASPL_{max}$, regardless of noise handling. A better understanding of this discrepancy can be gained when plotting the Pareto front between the design objectives $OASPL_{max}$ and η as shown in Fig. 12 and 13. The $crit_{comb}$ metric is additionally visualized as a contour plot.

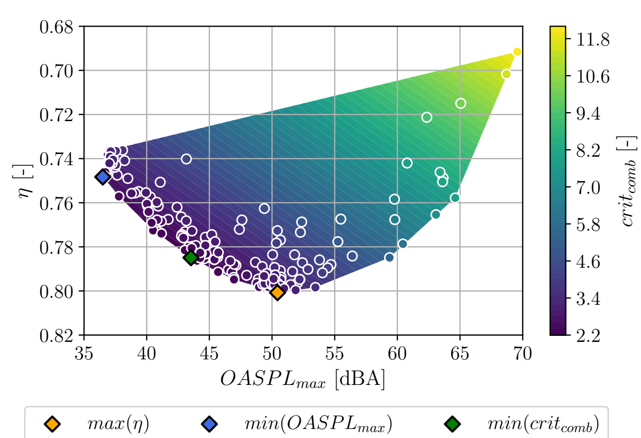

Figure 12. Pareto front: $OASPL_{max}$ vs. η with contour plot of combined criterion $crit_{comb}$

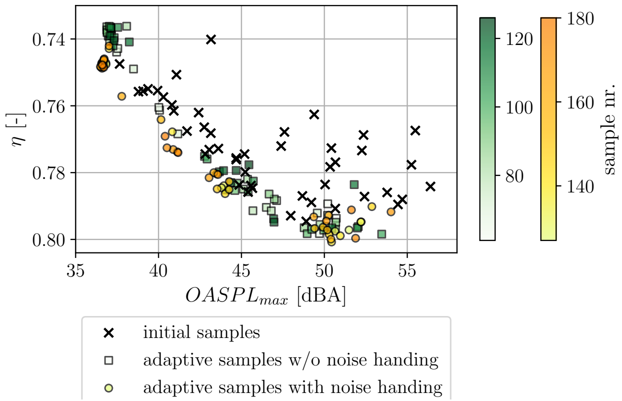

Figure 13. Pareto front: $OASPL_{max}$ vs. η with adaptive optimization progress visualized

The adaptive design points selected with and without noise handling are represented in the lower Pareto plot as rectangles and dots, respectively. A green and orange color scale is used to indicate the corresponding sample numbers and illustrate the optimization progress. A strong clustering of adaptive samples around the optimal $OASPL_{max}$ design point can be observed in the upper left corner of the Pareto plot. It is evident that the variance in η is larger than that in $OASPL_{max}$. The small variation of $OASPL_{max}$ near its optimum aligns with its lower prediction error compared to the other metrics. Without noise handling, the optimization of $OASPL_{max}$ appears to be stuck in a local minimum. However, once noise handling is enabled, a better solution is found, attributed to the enhanced prediction accuracy of the surrogate.
For η, on the other hand, design points are more sparsely distributed around the optimal η design point. Even after noise handling was included, some adaptive points still exhibit significantly worse η values than predicted, with a greater spread among the selected designs. This observation aligns with greater prediction error for η, indicating that the surrogate model overestimates the aerodynamic efficiency of the corresponding design points. Possible reasons for this include an insufficiently converged η optimum with too sparse exploration of the design space in the concerned region, or a general higher sensitivity of the η data.
Since $crit_{comb}$ is proportional to both η and $OASPL_{max}$, any uncertainty in η directly impacts the uncertainty in the combined criterion. Furthermore, while the regions around the optima of $OASPL_{max}$ and η are more condensed, there is a much larger area on the Pareto front where theoretically good candidates for $crit_{comb}$ could be found. This leads to a larger potentially feasible region in the design space for this objective, which remains less explored due to fewer data points. Therefore, it is reasonable to expect that more iterations are required to find a global optimum for the combined criterion $crit_{comb}$, compared to η or $OASPL_{max}$. The evolution of the current best value at each iteration from the evaluated dataset for each optimization objective is shown in Fig. 14.

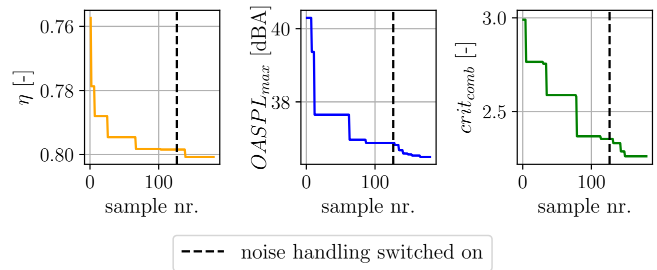

Figure 14. Optimization evolution of current best objective value of $OASPL_{max}$, η and $crit_{comb}$

Significant improvements are made for all three objectives throughout the adaptive optimization process. As noted earlier, once noise handling was introduced, additional enhancements were observed for each objective during the remaining optimization iterations. It is not guaranteed that the global optimization has fully converged yet, meaning there may still be room for further improvements. A larger number of design iterations is required to indicate global convergence of the optimization problem confidently.

To better understand the explored design space and the co-dependencies of the input parameters, the input parameters for each sample from the adaptive process are plotted against each other in Fig. 15, 16, and 17, corresponding to their respective objective functions, η, $OASPL_{max}$, and $crit_{comb}$. This shows some of the trends of the propeller geometry and the influence of the respective parameters on the different objectives. In general, the more concentrated good designs are around a certain value for a certain parameter, the higher the influence of that parameter on the concerned objective.

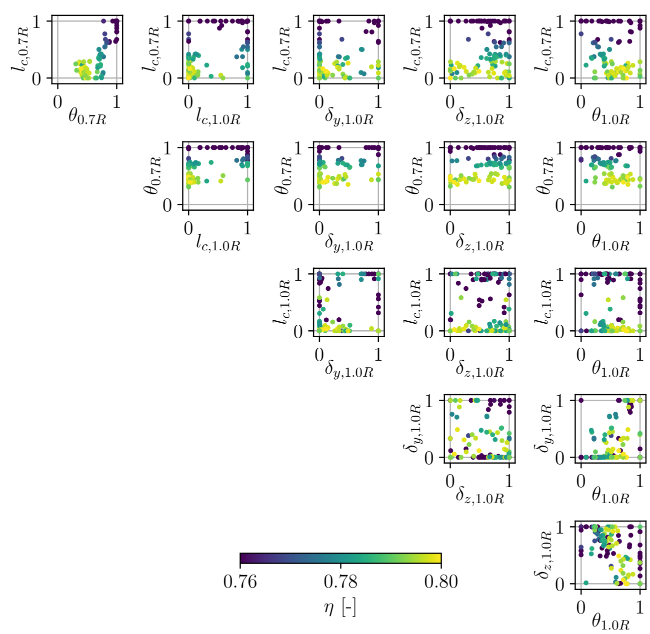

Figure 15. Parameter map of adaptive samples: efficiency η

For η, a concentrated distribution of well-performing designs is observed for $\theta_{0.7R}$ around the mid-range of its parameter definition. $l_{c,0.7R}$ is slightly more vastly distributed but still follows a clear trend, in its case towards values in the lower quarter fraction. The tip chord $l_{c,1.0R}$ also shows a strong tendency towards smaller values. While the tip sweep $\delta_{y,1.0R}$ is more broadly distributed across the range, there remains a tendency towards high sweep values. In contrast, the tip anhedral $\delta_{z,1.0R}$ shows a broader distribution with only a slight trend towards higher anhedral, indicating that it only has a little influence on the η for cruise flight condition. In summary, it appears that a design with a high propulsive efficiency is highly dependent on $l_{c,0.7R}$, $\theta_{0.7R}$, $l_{c,1.0R}$, while lower sensitivity with respect to $\delta_{y,1.0R}$ and $\delta_{z,1.0R}$.

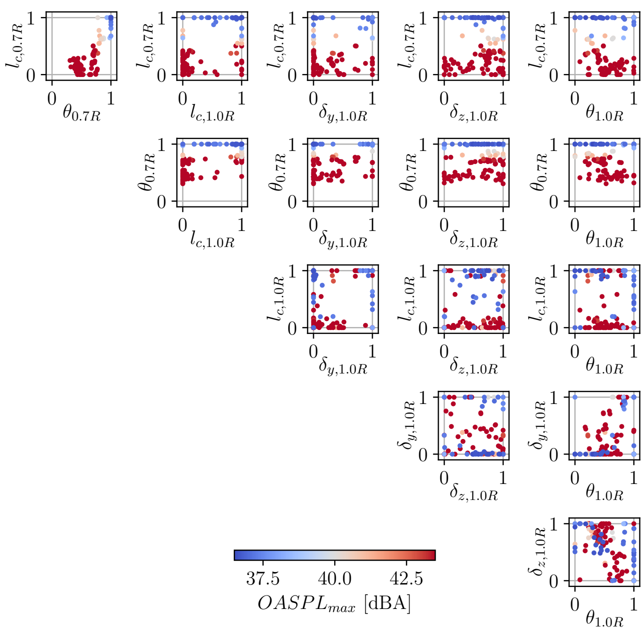

Figure 16. Parameter map of adaptive samples: $OASPL_{max}$

For $OASPL_{max}$, both $l_{c,0.7R}$ and $\theta_{0.7R}$ approach their upper design limit during the optimization process. The tip chord $l_{c,1.0R}$ has a slight tendency towards the upper limit, the tip sweep $\delta_{y,1.0R}$ towards the lower limit, and tip pitch $\theta_{1.0R}$ towards the lower mid field from its parameter range. The trend for $l_{c,1.0R}$, $\delta_{y,1.0R}$ and $\theta_{1.0R}$ is not as pronounced as for $l_{c,0.7R}$ and $\theta_{0.7R}$, and there are individual outliers which still achieve good results. This indicates a lower sensitivity of $l_{c,1.0R}$, $\delta_{y,1.0R}$ and $\theta_{1.0R}$ compared to $l_{c,0.7R}$ and $\theta_{0.7R}$. Tip anhedral $\delta_{z,1.0R}$ shows a slight trend towards values from the upper mid field. It is more vastly distributed, indicating only a small influence on $OASPL_{max}$. Therefore, the reduction of $OASPL_{max}$ is primarily driven by $l_{c,0.7R}$ and $\theta_{0.7R}$. This represents a situation where the objectives of reducing $OASPL_{max}$ and maximizing η are in direct opposition. Comparing Fig. 15 and 16 this argument can further be validated by the fact that the design points doing well in the $OASPL_{max}$ plot are the ones doing significantly worse in the η plot, and vice versa. This emphasizes the importance of the combined criterion to identify propeller designs that achieve the best possible trade-off between $OASPL_{max}$ and η.

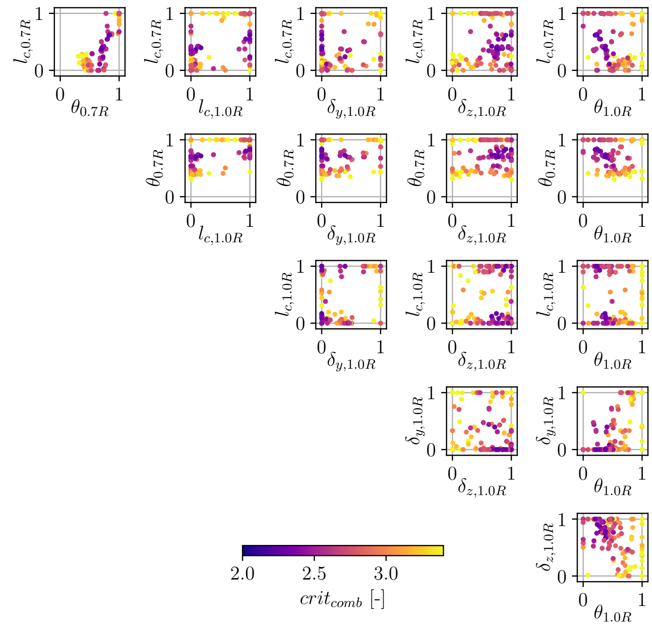

Figure 17. Parameter map of adaptive samples: Combined criterion $crit_{ccomb}$

For $crit_{comb}$, the sizing of $l_{c,0.7R}$ and $\theta_{0.7R}$ is now more moderate and good candidates lie in between the respective optima of $OASPL_{max}$ and η. Tip chord $l_{c,1.0R}$ is distributed more vastly with well-performing designs on both ends of the limit. This aligns with the behavior for $OASPL_{max}$ which did predominantly well for higher tip chord, and η which did well for low tip chord. Tip pitch $\theta_{1.0R}$ shows clustering slightly below the middle. As with the other two objectives, there is a tendency towards high tip sweep $\delta_{y,1.0R}$ for the $crit_{comb}$ as well. Tip anhedral $\delta_{z,1.0R}$ tends to lower values with the ideal design points clustering around the upper quarter of the parameter range.

Optimized Propeller Designs

In this section, the following three propeller designs, selected based on the three optimization criteria η, $OASPL_{max}$ and $crit_{comb}$, are presented and evaluated in detail:

- Sample nr. 139: $\max(\eta)$
- Sample nr. 166: $\min(OASPL_{max})$
- Sample nr. 149: $\min(crit_{comb})$

A rendering from the CAD model of the three propeller geometries is depicted in Fig. 18. The distribution of the geometric parameters across the blade radius is shown in Fig. 19. The design trends discussed in the previous section are also reflected in the optimization candidates.

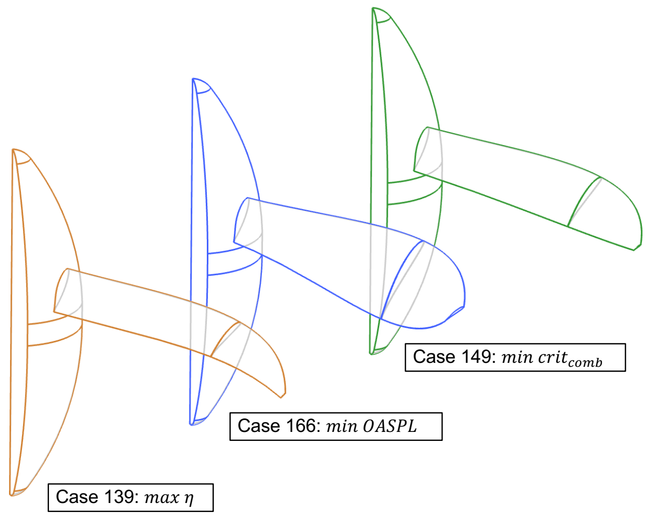

Figure 18. Isometric view of the three selected propeller designs: $\max(\eta)$**,** $\min(OASPL_{max})$ **and** $\min(crit_{comb})$

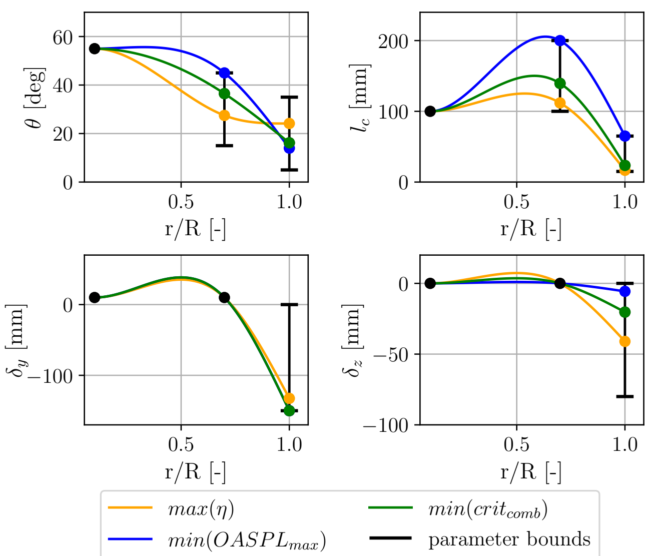

Figure 19. Geometric parameters of the three selected propeller designs: $\max(\eta)$**,** $\min(OASPL_{max})$ **and** $\min(crit_{comb})$

The $\max(\eta)$ propeller features a comparably lower pitch angle $\theta_{0.7R}$ and a higher tip pitch $\theta_{1.0R}$. In contrast, the quieter $\min(OASPL_{max})$ propeller exhibits the highest pitch $\theta_{0.7R}$, but a lower tip pitch $\theta_{1.0R}$. The $\min(crit_{comb})$ propeller falls between these two designs in terms of $\theta_{0.7R}$, and for $\theta_{1.0R}$ is very close to the $\min(OASPL_{max})$ design. Regarding chord distribution, the $\max(\eta)$ propeller maintains a consistently low chord along the blade radius, whereas the $\min(OASPL_{max})$ design reaches the maximum chord limit for the entire blade span. The chord distribution of the $\min(crit_{comb})$ propeller blade again falls in between the other two designs, slightly closer to the $\max(\eta)$ chord. All three designs feature a high blade tip sweep $\delta_{y,1.0R}$, indicating that a backward-swept propeller is beneficial for both the aeroacoustic and the aerodynamic performance. Moderate tip anhedral $\delta_{z,1.0R}$ provides some performance benefits. The $\max(\eta)$ propeller anhedral is right in the middle of the design range, while the $\min(OASPL_{max})$ design only has a slight anhedral. Once again, the $\min(crit_{comb})$ design lies in between the two other configurations.

To illustrate the characteristic flow fields of the optimized designs, isovorticity plots are used to visualize the vortex structures, as shown in Fig. 20.

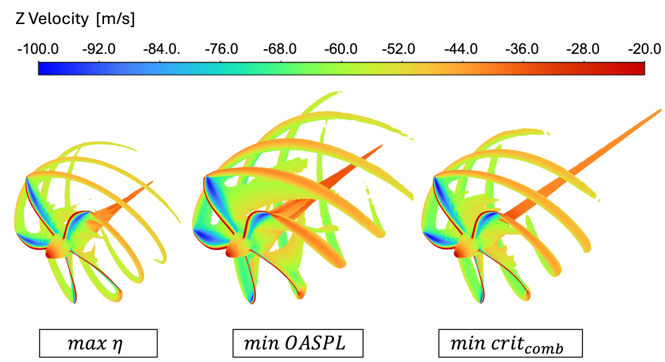

Figure 20. Isovorticity surfaces with z-velocity plot of the three selected propeller designs: $\max(\eta)$**,** $\min(OASPL_{max})$ **and** $\min(crit_{comb})$

It can be observed that the $\min(OASPL_{max})$ design generates the most dominant tip vortices, while the $\max(\eta)$ design produces the smallest. Furthermore, the different advance ratios also indicate the different rotational speeds associated with the designs. In general, a propeller featuring a smaller and less twisted blade surface has to rotate faster to produce the same thrust. This statement is confirmed as the bigger and more twisted $\min(OASPL_{max})$ blade rotates slower than the more narrow and less twisted $\max(\eta)$ blade. A higher rotational velocity increases the noise intensity, as the loading noise increases with the rate of change of the pressure distribution. Furthermore, a higher RPM shifts the emitted noise to higher frequencies which are penalized by the A-weighting. The flow field z-velocity in the plane of the propeller wake of the optimization geometries is depicted in Fig. 21. A small detachment zone near the blade root can be observed for the $\min(OASPL_{max})$ design. This detachment zone occurs due to the low circumferential velocity, which results in a high negative angle of attack at the blade root. The incoming flow is no longer able to follow the airfoil contour, leading to flow separation on the lower surface of the propeller blade.

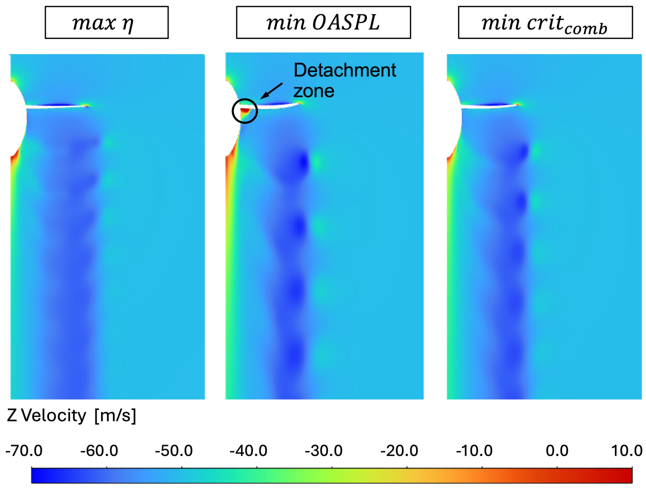

Figure 21. Z-velocity plot of propeller wake of the three selected propeller designs: $\max(\eta)$, $\min(OASPL_{max})$ and $\min(crit_{comb})$

For the $\min(crit_{comb})$ and $\max(\eta)$ cases, due to the higher RPM, the circumferential velocity is large enough at the blade root to prevent this. To further highlight this aspect, the local wall shear stress and the pressure distribution on the propeller blade surfaces are depicted in Fig. 22 and Fig. 23.

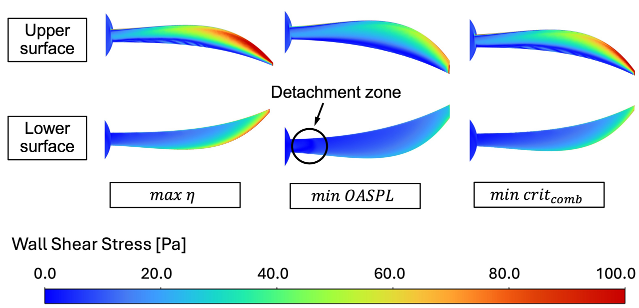

Figure 22. Wall shear stress on the propeller blade surfaces of the three selected propeller designs: $\max(\eta)$, $\min(OASPL_{max})$ and $\min(crit_{comb})$

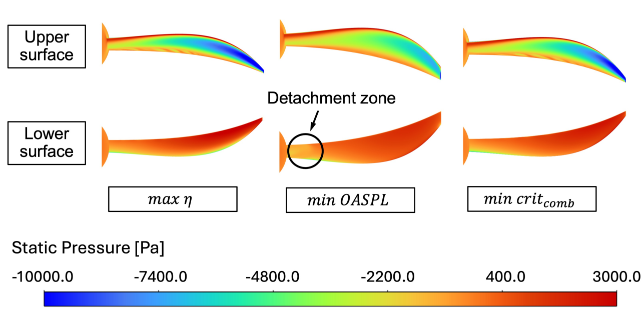

Figure 23. Local pressure on the propeller blade surfaces of the three selected propeller designs: $\max(\eta)$, $\min(OASPL_{max})$ and $\min(crit_{comb})$

Areas featuring a wall shear stress of 0 Pa indicate flow detachment on the surface. In all three designs, detachment of the flow on the upper surface near the trailing edge can be observed. This indicates that even for the optimized blade geometries, the local airfoil conditions are not fully ideal, suggesting further room for overall performance improvement by adjusting the airfoil geometry along the blade. Between the designs, local wall shear is highest for the $\max(\eta)$ design, which is reasonable as this blade design features the highest tip velocity. Furthermore, the detachment zone near the blade root of the $\min(OASPL_{max})$ blade is also slightly visible. The values in Fig. 23 show the pressure difference of the local static pressure and the reference pressure. Since all three designs generate the same total thrust, the pressure difference is greatest for the $\max(\eta)$ design, as it also features the smallest blade surface area. To highlight the impact of the flow separation, the pressure distribution of the $\min(OASPL_{max})$ blade lower surface is depicted in Fig. 24, with an adjusted value range for better visibility.

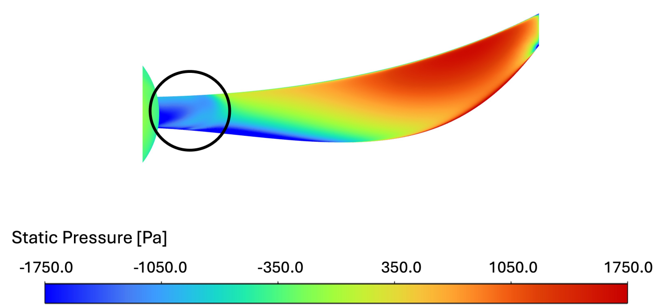

Figure 24. Flow detachment at blade root: pressure distribution of $\min(OASPL_{max})$ lower blade surface with an adjusted value range

Here, the exact location and size of the detachment region are more evident, characterized by an abrupt drop in static pressure at the blade root. This pressure drop acts as a suction force on the lower blade surface, counteracting the effective thrust of the overall propeller, leading to a slightly decreased efficiency of the propulsive force. This reduces the aerodynamic effectiveness of the inboard region, resulting in a more outward thrust distribution and an increased torque demand, resulting in higher power requirements.

The A-weighted OASPL values at the receiver positions are shown in Fig. 25. As expected, the OASPL level of the $\min(OASPL_{max})$ propeller is consistently the lowest for all receiver locations, $\max(\eta)$ the highest, and the $\min(crit_{comb})$ design is in the middle. Only a small directivity is present in the propeller noise distribution, where the corresponding maxima are found roughly at 100° relative to the axis of rotation. The OASPL values approach zero at 0° and 180° relative to the axis of rotation.

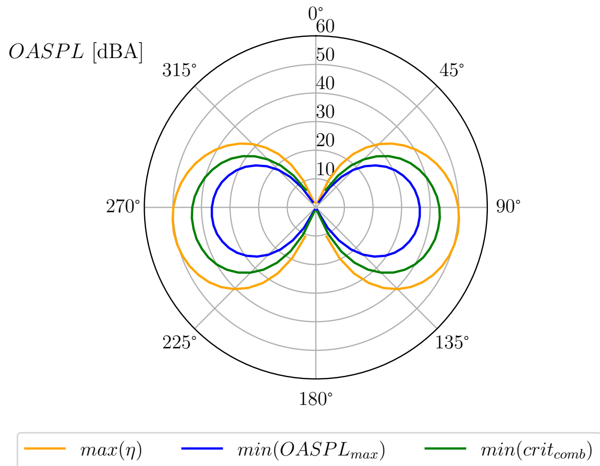

Figure 25. OASPL at receiver locations of the three selected propeller designs: $\max(\eta)$**,** $\min(OASPL_{max})$ **and** $\min(crit_{comb})$

Further insights into the different characteristics of the designs can be gained when analyzing the local forces and moments distributions. The local axial force T/r, the local tangential force Q/r^2 and the ratio between the two $\frac{T}{Q/r}$ are depicted in Fig. 26. To reduce loading noise, it is beneficial to shift blade loading inboard as much as possible. This approach reduces the magnitude of pressure fluctuations associated with loading noise. The reason for this is that, when looking at the used FWH formulation (see Equation 6), a larger portion of the blade loading is concentrated in a region where the rate of change of M_r (the Mach number component normal to the source, in this case the propeller blade) is smaller. This occurs because velocity is lower near the blade root, leading to a smaller amplitude of the change of M_r over one revolution. The $\min(OASPL_{max})$ design aims for the lowest RPM possible while still trying to push the load distribution as much inboard as possible. The design is already at the limit as the blade pitch is already at its maximum up to 0.7R, and therefore a more inboard loading could only be achieved at the cost of a higher rpm. Therefore, it can be concluded that the $\min(OASPL_{max})$ design prioritizes a low RPM as the main noise reduction mechanism, while maximizing inboard load distribution. Technically, the thickness noise would reduce with a smaller and more narrow blade tip. However, its overall impact is expected to be minimal, as thickness noise generally only becomes significant at Mach numbers above 0.7 (Ref. 18). A further reduction in the noise emission could be attained by including $\theta_{0.1R}$ as an optimization parameter, with the added benefit of also improving the efficiency. The $\max(\eta)$ design features the smallest resistant torque out of the three propellers. This is due to the narrower and less twisted blade generating less drag in operation. Additionally, by shifting the thrust more inboard, a more inward tangential force is achieved, further lowering the effective torque. Furthermore, a more inboard

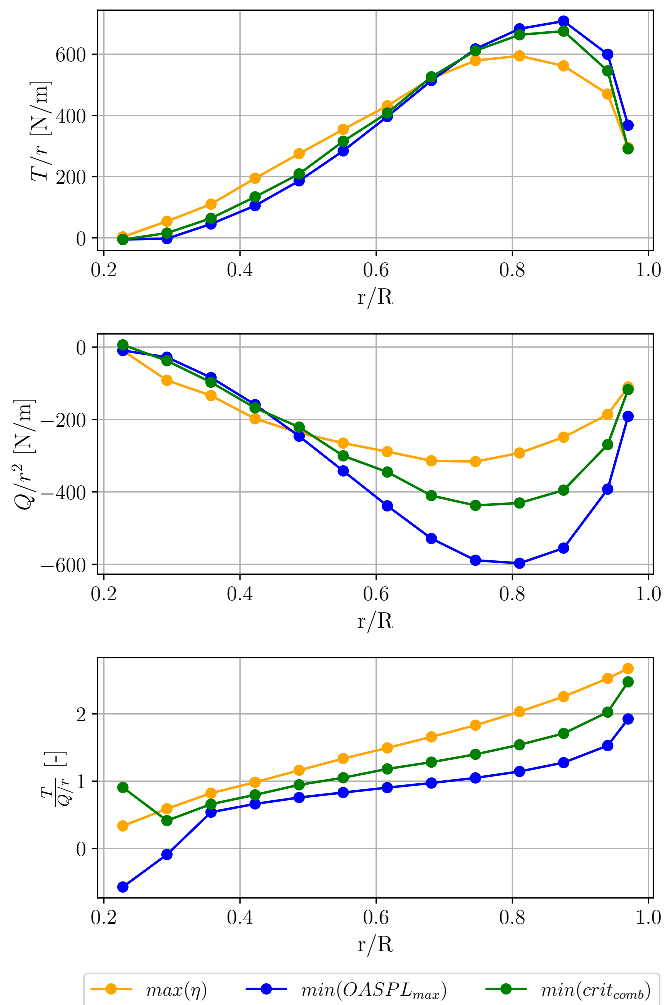

Figure 26. Local axial force, local tangential force and ratio between axial and tangential force along the blade of the three selected propeller designs: $\max(\eta)$**,** $\min(OASPL_{max})$ **and** $\min(crit_{comb})$

blade loading can as well improve efficiency by reducing tip vortex strength, as shifting high loading away from the tip decreases the local pressure difference between the upper and lower blade surfaces. This results in weaker vortex generation and lower induced drag of the propeller blade. The drag of the $\min(OASPL_{max})$ blade is significantly higher compared to the other designs, associated with the higher blade solidity. In combination with a more outboard loading characteristic, and while taking the propeller speed into account, this results in a higher power consumption and a lower propulsive efficiency. Once again, the $\min(crit_{comb})$ represents a trade-off between the other two designs. With a slightly more inboard loading compared to the $\min(OASPL_{max})$ design and a local tangential force and axial to tangential force ratio right in the middle between the $\min(OASPL_{max})$ and the $\max(\eta)$ design. The Table 5 summarizes the relevant numerical results from the optimization designs for the discussion.

Table 5. Results comparison of the three selected propeller designs: $\max(\eta)$, $\min(OASPL_{max})$ and $\min(crit_{comb})$

	$\max(\eta)$	$\min(OASPL_{max})$	$\min(crit_{comb})$	baseline geometry
RPM	1637.94	1039.07	1310.62	1757.43
Ma_{tip}	0.48	0.32	0.39	0.51
efficiency η [-]	0.8008	0.7483	0.7849	0.7756
$OASPL_{max}$ [dBA]	50.44	36.50	43.53	54.16
$crit_{comb}$ [-]	2.848	2.685	2.261	4.852

Compared to the baseline geometry, the $\max(\eta)$ propeller outperforms it in both aerodynamic efficiency and aeroacoustic noise emission. The $\min(OASPL_{max})$ design is less efficient than the baseline but achieves a significant tonal noise reduction of nearly 18 dBA. Meanwhile, the $\min(crit_{comb})$ propeller offers slightly higher efficiency than the baseline while still providing a notable OASPL reduction of 10 dBA.

CONCLUSIONS

The main results of this study can be summarized as the following:

1. A surrogate-based multi-objective optimization framework was successfully applied to an eVTOL propeller in cruise, simultaneously minimizing tonal noise emissions and maximizing aerodynamic efficiency.
2. The propeller blade, parameterized with six geometric variables, was analyzed using steady-state RANS CFD for aerodynamics and the Ffowcs-Williams–Hawkings method for aeroacoustics.
3. An initial Latin Hypercube sample of 60 designs, followed by 20 adaptive infill iterations adding 120 designs, enabled the surrogate model to balance exploration and exploitation effectively across the design space.
4. Three optimized candidates, each best with respect to tonal-noise reduction, aerodynamic efficiency, and the combined trade-off metric, outperformed the baseline propeller.
5. Incorporating data noise handling into the surrogate model notably enhanced both its predictive accuracy and the overall efficiency of the optimization process.
6. The study demonstrates that SBO can be feasibly integrated into industrial propeller design workflows involving expensive CFD evaluations, though robust automated meshing across diverse geometries remains a key challenge.

For future work, the following aspects could further enhance the optimization process:

1. Incorporating a broadband prediction model for far-field noise emissions would allow for a more accurate representation of the actual propeller noise emissions.
2. Expanding the number of optimization parameters would also enable a more comprehensive analysis by considering additional geometric effects.
3. Considering multiple flight states beyond purely axial inflow would provide a more realistic and versatile evaluation of design performance across a typical flight envelope

Author contact: Elias Peter elias.peter@tum.de, Jan-Arun Faust faust@erc-system.com, Marco Stuhlpfarrer stuhlpfarrer@erc-system.com

REFERENCES

1. Doo, J. T., Tsairides, M. A., Pavel, M. D., Smith, M., Didey, A., Bennet, E., Hange, C., Bromfield, M., Diller, N. P., and Mooberry, J., “NASA Electric Vertical Takeoff and Landing (eVTOL) Aircraft Technology for Public Services—A White Paper,” NASA Technical Paper NASA/TP-20205000636, NASA Transformative Vertical Flight Working Group 4, 2021.
2. “ERC Webpage,” ERC-System GmbH, Available: https://www.erc-system.com, Accessed: 3 March 2025.
3. Greenwood, E., Brentner, K. S., Rau, R. F., and Gan, Z. F. T., “Challenges and Opportunities for Low Noise Electric Aircraft,” *International Journal of Aeroacoustics*, Vol. 21, (5-7), 2022, pp. 315–381. DOI: 10.1177/1475472X221107377.
4. “eVTOL Aircraft Directory,” Vertical Flight Society, Available: https://evtol.news/aircraft, Accessed: 7 January 2025.
5. “Volocopter Webpage,” Volocopter, Available: https://www.volocopter.com, Accessed: 13 January 2025.
6. “Joby Webpage,” Joby Aviation, Available: https://www.jobyaviation.com/, Accessed: 13 January 2025.
7. Leishman, J. G., *Principles of Helicopter Aerodynamics*, Cambridge University Press, ISBN: 978-1107013353, 2016, pp. 115–152.

8. Higgins, R. J., Barakos, G. N., Shahpar, S., and Tristanto, I., "A Computational Fluid Dynamic Acoustic Investigation of a Tiltwing eVTOL Concept Aircraft," *Aerospace Science and Technology*, Vol. 111, 2021, pp. 106571. DOI: 10.1016/j.ast.2021.106571.

9. Zhang, T., Barakos, G. N., Furqan, and Foster, M., "High-Fidelity Aerodynamic and Acoustic Design and Analysis of a Heavy-Lift eVTOL," *Aerospace Science and Technology*, Vol. 137, 2023, pp. 108307. DOI: 10.1016/j.ast.2023.108307.

10. Thai, A., Bain, J., Mikic, G., and Stoll, A., "Flyover Noise Computations of the Joby Aviation Aircraft," Proceedings of the Vertical Flight Society 79th Annual Forum, West Palm Beach, FL, 2023, Paper No. F-0079-2023-17959. DOI: 10.4050/F-0079-2023-17959.

11. Klimczyk, W., and Sieradzki, A., "RANS-Based Aeroacoustic Global Sensitivity Study and Optimization of UAV Propellers," *Aerospace*, Vol. 10, (3), 2023, pp. 306. DOI: 10.3390/aerospace10030306.

12. Marinus, B., Roger, M., and Van Den Braembussche, R., "Aeroacoustic and Aerodynamic Optimization of Aircraft Propeller Blades," 16th AIAA/CEAS Aeroacoustics Conference, Stockholm, Sweden, 2010, Paper No. AIAA-2010-3850. DOI: 10.2514/6.2010-3850.

13. Yu, P., Peng, J., Bai, J., Han, X., and Song, X., "Aeroacoustic and Aerodynamic Optimization of Propeller Blades," *Chinese Journal of Aeronautics*, Vol. 33, (3), 2020, pp. 826–839. DOI: 10.1016/j.cja.2019.11.005.

14. Weitsman, D., and Greenwood, E., "Parametric Study of eVTOL Rotor Acoustic Design Trades," AIAA SciTech 2021 Forum, Virtual Event, 2021, Paper No. AIAA-2021-1987. DOI: 10.2514/6.2021-1987.

15. Bain, J., Stoll, A., and Mikic, G., "Aerodynamic and Acoustic Design of the Joby Aviation eVTOL Propeller," Proceedings of the 77th Annual Forum & Technology Display, Virtual Event, 2021, Paper No. F-0077-2021-16687. DOI: 10.4050/F-0077-2021-16687.

16. Hepperle, M., "Aerodynamics of Model Aircraft, Other Airfoils," URL: Available: https://www.mh-aerotools.de/airfoils/ Accessed: 13 January 2025.

17. ANSYS Inc., *ANSYS 24R1 Theory Guide*, Canonsburg, PA, 2024.

18. Glegg, S., and Devenport, W., *Aeroacoustics of Low Mach Number Flows: Fundamentals, Analysis and Measurement*, Academic Press, Oxford, UK, ISBN: 978-0-12-809651-2, 2017, pp. 95–114.

19. Rizzi, S., Huff, D., Bent, P., Henderson, B., Pascioni, K., Sargent, D., Josephson, D., Marsan, M., He, H., and Snider, R., "Urban Air Mobility Noise: Current Practice, Gaps, and Recommendations," NASA Technical Paper NASA TP–2020-5007433, NASA, 2020.

20. Brooks, T., Pope, D., and Marcolini, M., "Airfoil Self-Noise and Prediction," Technical Report Reference Publication 1218, NASA, 1989.

21. Gramacy, R. B., *Surrogates: Gaussian Process Modeling, Design and Optimization for the Applied Sciences*, Chapman & Hall/CRC, Boca Raton, FL, 2020, pp. 118 – 138.

22. Forrester, A. I. J., and Keane, A. J., "Recent Advances in Surrogate-Based Optimization," *Progress in Aerospace Sciences*, Vol. 45, (1–3), 2009, pp. 50–79. DOI: 10.1016/j.paerosci.2008.11.001.

23. Hu, W., *Design Optimization Under Uncertainty*, Springer, 2023, pp. 65–90. DOI: 10.1007/978-3-031-49208-2.

24. Seeger, M., "Gaussian Processes for Machine Learning," *International Journal of Neural Systems*, Vol. 14, (2), 2004, pp. 69–106. DOI: 10.1142/S0129065704001899.

25. Ankenman, B., Nelson, B. L., and Staum, J., "Stochastic Kriging for Simulation Metamodeling," *Operations Research*, Vol. 58, (2), 2010, pp. 371–382. DOI: 10.1287/opre.1090.0754.

26. Saves, P., Lafage, R., Bartoli, N., Diouane, Y., Bussemaker, J., Lefebvre, T., Hwang, J. T., Morlier, J., and Martins, J. R. R. A., "SMT 2.0: A Surrogate Modeling Toolbox with a Focus on Hierarchical and Mixed Variables Gaussian Processes," *Advances in Engineering Software*, Vol. 188, 2024, pp. 103571. DOI: 10.1016/j.advengsoft.2023.103571.

27. Jones, D. R., Schonlau, M., and Welch, W. J., "Efficient Global Optimization of Expensive Black-Box Functions," *Journal of Global Optimization*, Vol. 13, (4), 1998, pp. 455–492. DOI: 10.1023/A:1008306431147.

28. Loeppky, J. L., Sacks, J., and Welch, W. J., "Choosing the Sample Size of a Computer Experiment: A Practical Guide," *Technometrics*, Vol. 51, (4), 2009, pp. 366–376. DOI: 10.1198/TECH.2009.08040.

29. Virtanen, P., Gommers, R., Oliphant, T. E., Haberland, M., Reddy, T., Cournapeau, D., Burovski, E., Peterson, P., Weckesser, W., Bright, J., van der Walt, S. J., Brett, M., Wilson, J., Millman, K. J., Mayorov, N., Nelson, A. R. J., Jones, E., Kern, R., Larson, E., Carey, C. J., Polat, İ., Feng, Y., Moore, E. W., VanderPlas, J., Laxalde, D., Perktold, J., Cimrman, R., Henriksen, I., Quintero, E. A., Harris, C. R., Archibald, A. M., Ribeiro, A. H., Pedregosa, F., van Mulbregt, P., and SciPy 1.0 Contributors, “SciPy 1.0: Fundamental Algorithms for Scientific Computing in Python,” *Nature Methods*, Vol. 17, (3), 2020, pp. 261–272. DOI: 10.1038/s41592-019-0686-2.